IEEE Access
Multidisciplinary | Rapid Review | Open Access Journal

Received August 27, 2020, accepted September 17, 2020, date of publication September 23, 2020,
date of current version November 27, 2020.

Digital Object Identifier 10.1109/ACCESS.2020.3026040

Multi-Objective Optimization of Double Primary Tubular Permanent Magnet Synchronous Linear Motor in Wide Temperature Range Environment Based on Pareto Front Method

ZHENYANG HAO[1], (Member, IEEE), WENSHUAI ZHOU[1], TIANPENG JI[1], XUZHEN HUANG[1], (Member, IEEE), AND CHENGMING ZHANG[2], (Member, IEEE)

[1]Department of Electrical Engineering, Nanjing University of Aeronautics and Astronautics, Nanjing 211106, China
[2]Department of Electrical Engineering, Harbin Institute of Technology, Harbin 150001, China

Corresponding author: Zhenyang Hao (zhenyang_hao@nuaa.edu.cn)

ABSTRACT In order to improve the thrust density of the electric actuator in aircraft, a double primary tubular permanent magnet synchronous linear motor is designed. By establishing the magnetic circuit model, the air gap magnetic density and thrust characteristics of outer and inner primary motors are analyzed. Considering that it works in the wide temperature range environment, a multi-objective optimization of motor is carried out. The surrogate model established by neural network is used to simplify the mathematical model of the motor. In order to improve the average thrust, restrain the thrust fluctuation and reduce the difference of output thrust under different environment temperatures, the Pareto front method is used to determine the target range of the optimal parameters, and gradually strengthen conditions, so as to obtain the optimal scheme of motor design.

INDEX TERMS Permanent magnet synchronous linear motor, multi-objective optimization, Pareto front method, wide temperature range environment.

I. INTRODUCTION

Aerospace electric actuators require motors with high thrust density. For the electric actuator with tubular linear motor, it is usually necessary to increase the external diameter of the motor in order to increase the thrust. With the increase of external diameter, the hollow volume inside the tubular linear motor expands, resulting in space waste. Therefore, the scheme of double primary tubular permanent magnet synchronous linear motor (DPT-PMSLM) is adopted. As shown in Fig.1, the motor employs two primaries with slot-less windings, one secondary formed by ring permanent magnet and iron core, and two air gaps. The primary inside and outside is stator, and the secondary part is mover. The outer and inner primary windings are excited by sinusoidal current at the same time, and the magnetic field generated by permanent magnet and the electrified windings generate the force to drive the secondary movement. The structure can improve the utilization rate of the internal space of the motor in a limited volume, so as to improve the thrust of the motor [1], [2]. In addition, the motor system working in the space environment has a wide range of temperature changes due to the influence of flight altitude of the aircraft, the change of daylight illumination and the temperature rise of its own operation. Also, it is difficult to use conventional ground cooling system to dissipate heat. Therefore, the motor is required to be adaptable to a wide temperature range environment.

Due to the complexity of structural parameters of DPT-PMLSM, it is difficult to obtain satisfactory results by using traditional optimization methods. So it is necessary to adopt some optimization algorithms which can considering complex multi parameters to optimize the thrust performance. For instance, in [3], considering the six objectives of the motor, a flux switching motor is optimized by Taguchi-Chicken Swarm Optimization method. In [4], the improved particle swarm optimization algorithm is used to optimize the permanent magnet of the embedded motor to reduce the

The associate editor coordinating the review of this manuscript and approving it for publication was Kai Li.

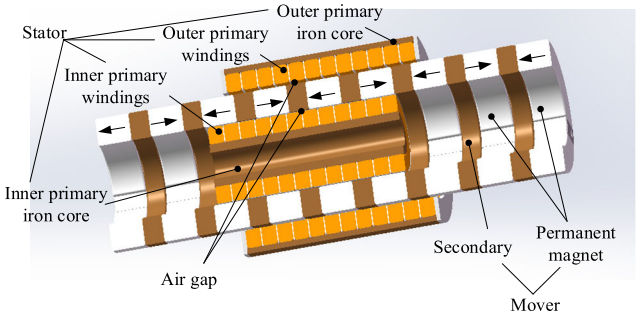

FIGURE 1. Topology of DPT-PMSLM.

harmonic content of the back EMF of the motor, adjust the number of particles in the optimization process, and improve the optimization efficiency.

The methods above are carried out after the completion of the mathematical model of the system, and the final optimization results are closely related to the accuracy of the established mathematical model. If the structure of the motor is relatively simple, a more accurate mathematical approximate model can be obtained. But in fact, due to the complex structure of the motor, it cannot be expressed by mathematical expression. The performance parameters of the motor are often obtained by slow FEA method, which requires a lot of screening. Therefore, the idea of surrogate model comes into being. Although surrogate model is less used in motor, it has been used in other multi parameter model optimization. A surrogate model is established by using response surface to optimize the size of the underwater glider, and the optimal parameters are selected by minimizing the error of the global multi response surface [5]. A surrogate model based on BP neural network is used to optimize the antenna, and all the structural parameters of the antenna transmitter are considered [6]. In [7], a new fault diagnosis method based on optimal wavelet tree and predator-prey search genetic algorithm to optimize neural network is proposed, which can accurately and timely identify and eliminate the stator turn to turn short circuit fault of induction motor. In [8], considering cross coupling and nonlinearity, the relationship between flux and current of permanent magnet synchronous reluctance motor is discussed with radial basis neural network.

With the expansion of motor application and the continuous improvement of motor performance, the optimization of motor also develops from single-objective to multi-objective. In the single-objective optimization, there is usually only one optimal solution, and it can be obtained by simple mathematical methods. However, in the multi-objective optimization, it is difficult to achieve balance in that the mutual constraints of each target may make the performance improvement of one target at the cost of losing other target performance. There cannot be a solution that optimizes all target performance. The common methods to solve multi-objective optimization problems are weighting method, response surface method and Pareto front method. In [9], [10], a multi-objective problem is transformed into a single objective problem by using the weighting method, and then the heuristic algorithm is used to get the optimal result. In [11], several reliability indexes of turbine rotor are considered, and geometrical parameters, material parameters and load parameters of rotor are optimized by response surface method Genetic algorithm can be used to find Pareto front [12], [13], but it will bring the calculation pressure.

This paper focuses on the multi-objective optimization design of DPT-PMSLM in a wide temperature range environment. Firstly, considering the particularity of structure, the magnetic circuit model is established, and the air gap magnetic density and thrust characteristics of outer and inner primary motors are analyzed. Secondly, a surrogate model based on neural network is used to predict the average thrust and thrust fluctuation of the motor. Different neural network models are trained under different working temperatures. Then the pareto front at different temperatures is obtained, and the optimal solution is obtained under a variety of constraints. Finally, a prototype was developed for experimental verification.

TABLE 1. Initial parameters of DPT-PMSLM.

parameters	Symbols	Units	Values
External diameter of DPT-PMSLM	D_1	mm	100
Inner diameter of outer primary yoke	D_1'	mm	92
Thickness of outer primary winding	h_{c1}	mm	9
Pole pitch	τ	mm	25.5
Thickness of permanent magnet	τ_m	mm	16.5
External diameter of secondary	D_m	mm	72
Inner diameter of secondary	D	mm	43
Thickness of inner primary winding	h_{c2}	mm	9
External diameter of inner primary yoke	D_2	mm	23
Inner diameter of DPT-PMSLM r	D_2'	mm	17
Outer primary physical air gap	g_1	mm	10
Inner primary physical air gap	g_2	mm	10

II. ELECTROMAGNETIC AND THRUST CHARACTERISTICS OF DPT-PMSLM

DPT-PMSLM studied in this paper adopts a slot-less structure to eliminate the influence of cogging force and reduce the machining difficulty. Windings are made into circular coils arranged in a certain phase sequence and fixed in the primary core. This structure also has the characteristics of good sinusoidal air gap magnetic density [14]. The initial parameters of DPT-PMSLM are shown in Table 1.

In this paper, the electromagnetic and thrust characteristics of DPT-PMSLM are studied by the equivalent magnetic circuit and FEA method, which provide a theoretical basis for the subsequent motor design.

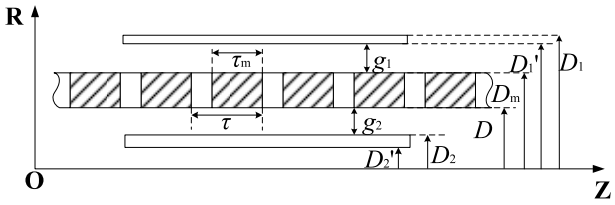

FIGURE 2. Parameter identification diagram of DPT-PMSLM (windings hidden).

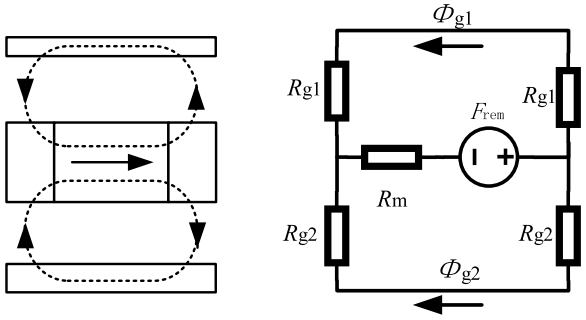

FIGURE 3. Equivalent magnetic circuit model of DPT-PMSLM.

A. MAGNETIC CIRCUIT MODEL AND ELECTROMAGNETIC CHARACTERISTICS

In order to facilitate the analysis, assume that the magnetic circuit model of DPT-PMSLM is as follows [15], [16]:

(1) the magnetic circuit is linear, the permeability of iron core is infinite, the influence of magnetic circuit saturation, hysteresis, eddy current is ignored, and the core loss is ignored;

(2) the permanent magnet has no magnetic flux leakage and no magnetic voltage drop;

(3) the influence of the end effect is not considered.

Fig.2 shows the parameter identification diagram of DPT-PMSLM, and Fig.3 shows the equivalent magnetic circuit model of DPT-PMSLM.

The equivalent magnetic potential of the permanent magnet F_{rem} can be calculated by

$$F_{rem} = \frac{B_{rem}\tau_m}{\mu_{rec}\mu_0} \tag{1}$$

where B_{rem} is the remanence, μ_{rec} is the relative permeability, and μ_0 is the vacuum permeability.

The magnetoresistance of the permanent magnet R_m can be calculated by

$$R_m = \frac{\tau_m}{\mu_{rec}\mu_0\frac{\pi}{4}(D_m^2 - D^2)} \tag{2}$$

The magnetoresistance of the outer primary air gap R_{g1} and that of the inner primary air gap R_{g2} are calculated respectively by

$$\begin{cases} R_{g1} = \dfrac{g_1}{\mu_0\dfrac{\tau - \tau_m + 2g_1}{2}\pi D_1'} \\ R_{g2} = \dfrac{g_2}{\mu_0\dfrac{\tau - \tau_m + 2g_2}{2}\pi D} \end{cases} \tag{3}$$

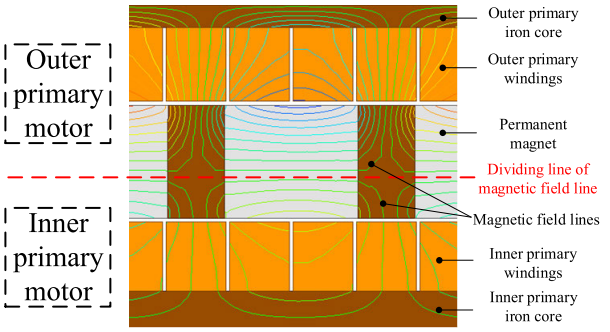

FIGURE 4. Distribution of magnetic field lines.

One part of the permanent magnet flux passes through outer air gap and the other part passes through inner air gap. The total flux Φ_{rem} is

$$\Phi_{rem} = B_{rem}\frac{\pi}{4}(D_m^2 - D^2) \tag{4}$$

From the equivalent magnetic circuit model and magnetic flux continuity, the following formulas can be obtained as

$$\begin{aligned} F_{rem} &= \Phi_{rem}R_m \\ &= 2\Phi_{g1}R_{g1} + (\Phi_{g1} + \Phi_{g2})R_m \\ &= 2\Phi_{g2}R_{g2} + (\Phi_{g1} + \Phi_{g2})R_m \end{aligned} \tag{5}$$

$$\Phi_{rem} = \Phi_{g1} + \Phi_{g2} \tag{6}$$

The magnetic fluxes of outer primary air gap Φ_{g1} and that of inner primary air gap Φ_{g2} are calculated by the following formulas respectively as

$$\begin{cases} \Phi_{g1} = \Phi_{rem}\dfrac{R_mR_{g2}}{2R_{g1}R_{g2} + R_m(R_{g1} + R_{g2})} \\ \Phi_{g2} = \Phi_{rem}\dfrac{R_mR_{g1}}{2R_{g1}R_{g2} + R_m(R_{g1} + R_{g2})} \end{cases} \tag{7}$$

The magnetic density formulas of outer primary air gap B_{g1} and that of inner primary air gap B_{g2} are derived as (8), as shown at the bottom of the next page.

Then, the distribution of magnetic field of the DPT-PMSLM shown in Fig. 4 is analyzed. When the influence of the end effect is ignored, the magnetic field distributions of the outer and inner primary motors are separated and form loops. Therefore, the outer primary motor and inner primary motor are weakly coupled. If the coupling between outer primary motor and inner primary motor is ignored, it can be considered that they can be analyzed independently, and the equivalent magnetic circuit model of them can also be calculated separately, as shown in Fig.5.

In order to calculate directly with Fig.5, it is necessary to know the distribution of permanent magnet source in two unit motors, that is, the ratio of F_{rem1} to F_{rem2} and the ratio of R_{m1} to R_{m2}, which can be expressed as

$$\begin{aligned} &F_{\mathrm{reml}}/F_{\mathrm{rem2}} \\ &= \frac{\tau_m g_2^2 D_1^2 - \frac{\mu_{rec}g_1^2 g_2 D(D_m^2 - D^2)}{\tau - \tau_m + 2g_1}}{\frac{\mu_{rec}g_1 g_2^2 D_1'(D_m^2 - D^2)}{\tau - \tau_m + 2g_2} - \tau_m g_1^2 D^2} \end{aligned} \tag{9}$$

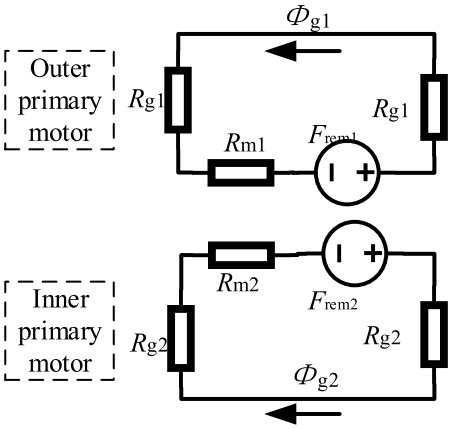

FIGURE 5. Layered equivalent magnetic circuit model.

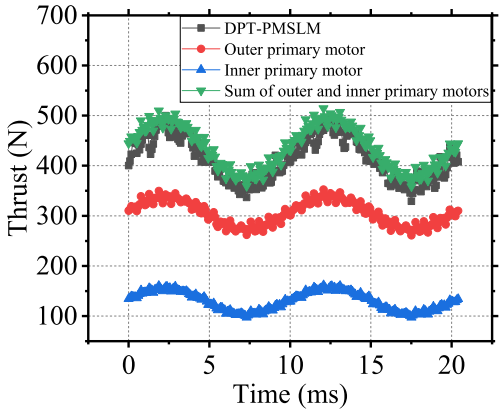

FIGURE 6. Motor thrust waveform.

$$\frac{R_{m1}}{R_{m2}} = \frac{\mu_{rec} g_1 g_2 \left(D_m^2 - D^2\right) - \tau_m g_2 \left(\tau - \tau_m + 2g_1\right) D_1}{\tau_m g_1 \left(\tau - \tau_m + 2g_2\right) D - \mu_{rec} g_1 g_2 \left(D_m^2 - D^2\right)} \quad (10)$$

In summary, Fig. 3 and Fig. 5 are two methods of building equivalent magnetic circuit models. Fig. 3 can be used to analyze various double primary motors. Fig.5 can only be used to analyze double primary motors with weak coupling between outer primary motor and inner primary motor, which will be described in detail in section B.

B. THRUST CHARACTERISTICS

Outer primary motor and inner primary motor both participate in the output thrust, and the total thrust can be obtained by superposing those thrust. The basic wave of back EMF and thrust of outer primary motor and inner primary motor can be calculated as

$$\begin{cases} E_1 = 4.44 f k_{w1} W_1 \Phi_{g1} \\ F_1 = \dfrac{3 E_1 I \sin \gamma_1}{2 f \tau} \end{cases} \quad (11)$$

$$\begin{cases} E_2 = 4.44 f k_{w2} W_2 \Phi_{g2} \\ F_2 = \dfrac{3 E_2 I \sin \gamma_2}{2 f \tau} \end{cases} \quad (12)$$

where E_1 and E_2 are the back EMF of outer primary motor and inner primary motor respectively, F_1 and is F_2 are thrust, f is frequency, k_{w1} and k_{w2} are the fundamental winding factor, W_1 and W_2 are the number of winding turns, and γ_1 and γ_2 are the phase difference of the electric Angle.

According to the specified volume and output thrust requirements, the initial parameters of DPT-PMSLM shown in Table 1 are determined through the above equivalent magnetic circuit analysis.

Then the FEA model of DPT-PMSLM is established according to the obtained initial parameters, and the thrust waveform is shown in Fig.6. DPT-PMSLM's thrust is 414.45 N, outer primary motor's thrust is 305.46 N and inner primary motor's thrust is 129.84 N. The sum of outer and inner primary motors' thrust is slightly higher than DPT-PMSLM's thrust. As a result, the thrust of double primary motor is increased by about 35.68% compared with outer primary motor, which shows the advantage of DPT-PMSLM. Thrust fluctuation of DPT-PMSLM is 171.65 N, and thrust fluctuation rate is about 41.4%, which affects the operation accuracy and control difficulty. Therefore, it is necessary to restrain thrust fluctuation later.

DPT-PMSLM's pole adopts ring-shaped and axial magnetization permanent magnet structure, as shown in Fig.7. The parameters of permanent magnet mainly include thickness, ring width and external diameter.

Increasing the thickness means that the amount of permanent magnet will increase when the other motor parameters remain unchanged, so the average thrust of motor will continue to increase [17]. In this paper, the thrust characteristics of DPT-PMSLM are studied by changing the ring width and the external diameter of permanent magnet. It should be noted that the external diameter of permanent magnet changes with inner diameter of outer primary motor, and the difference between them is the thickness of an air gap.

It can be seen from Fig.8 that thrust of DPT-PMSLM is related to the amount of permanent magnet. The wider the ring width, the greater the thrust. However, when the ring width is more than 15mm, the thrust of DPT-PMSLM increases at a turning point and the increase amplitude

$$\begin{cases} B_{g1} = \dfrac{\Phi_{g1}}{\pi D_1' \tau_f} = \dfrac{B_{rem}}{4} \dfrac{\tau_m g_2 (D_m^2 - D^2)}{\mu_{rec} g_1 g_2 (D_m^2 - D^2) + \tau_m (\tau - \tau_m)(D g_1 + D_1' g_2)} \\ B_{g2} = \dfrac{\Phi_{g2}}{\pi D \tau_f} = \dfrac{B_{rem}}{4} \dfrac{\tau_m g_1 (D_m^2 - D^2)}{\mu_{rec} g_1 g_2 (D_m^2 - D^2) + \tau_m (\tau - \tau_m)(D g_1 + D_1' g_2)} \end{cases} \quad (8)$$

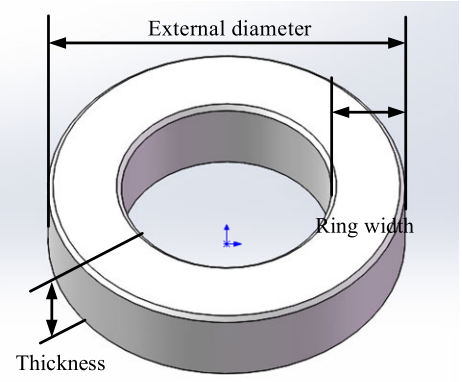

FIGURE 7. Schematic diagram of permanent magnet parameters.

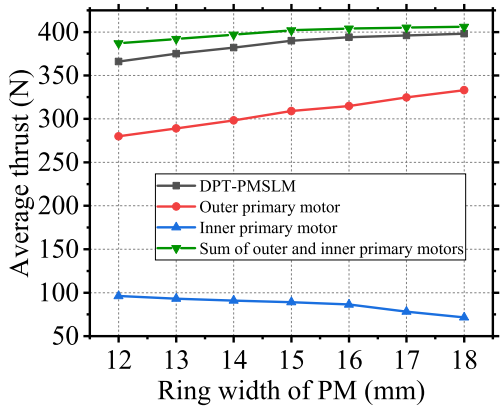

FIGURE 8. Motor thrust varies with ring width of PM.

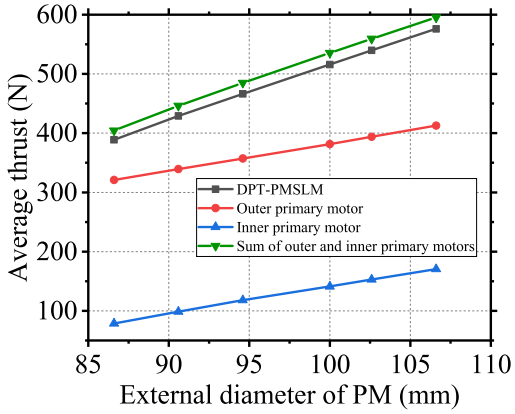

FIGURE 9. Motor thrust varies with external diameter of PM.

decreases. Correspondingly, as the external diameter of inner primary motor decreases, the thrust of it gradually decreases. What's more, with the increase of ring width, the difference between DPT-PMSLM's thrust and the sum of outer and inner primary motors' thrust decreases gradually. This shows that the larger the ring width of PM, the weaker the coupling between outer primary and inner primary motors. Due to the layered equivalent magnetic circuit model of Fig.5 proposed in part A is obtained by the weak coupling inside and outside, it can be further concluded that the model in Fig.5 is more suitable for DPT-PMSLM with large ring width.

And it can be seen from Fig.9 that, when the external diameter of PM increases, the thrust of outer and inner primary

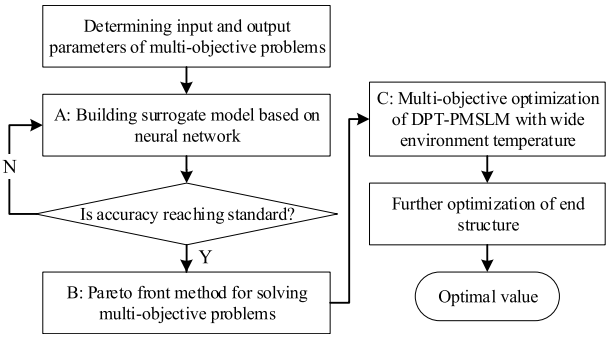

FIGURE 10. Optimization flow chart.

motors both gradually increase, which together promote the thrust increase of DPT-PMSLM. What's more, the larger the external diameter, the larger the proportion of inner primary motor thrust in DPT-PMSLM thrust. This shows that, in large external diameter applications, adding inner primary can effectively increase the internal space utilization of the motor and achieve the goal of high thrust density. When the external diameter of PM is less than 85 mm, double primary structure has little effect on increasing the thrust, but increase manufacturing difficulty.

III. THRUST OPTIMIZATION BASED ON PARETO FRONT

It is difficult to optimize the design because of the complexity of structural parameters. In this paper, the surrogate model is established based on neural network. DPT-PMSLM is optimized based on Pareto front method. The neural network can be trained by the FEA results, so as to predict the results of other possible schemes, greatly reducing the calculation time. Pareto front method transforms the multi-objective optimization problem into multi-group double objective optimization problems, which reduces the difficulty of motor performance evaluation. Fig.10 shows the overall optimization flow chart.

A. BUILDING SURROGATE MODEL BASED ON NEURAL NETWORK

In order to connect some structural parameters of DPT-PMSLM with the thrust performance, the neural network is used to build the surrogate model. In DPT-PMSLM, some parameters that need to be optimized are selected as the input of surrogate model, and the output parameters are average thrust and thrust fluctuation which can measure the thrust performance. The main structure diagram of the method is shown in Fig.11.

The input layer of neural network is seven neurons with structure parameters, the hidden layer is a large number of neuron nodes, and the output layer is two neurons with motor thrust performance. The two adjacent layers of neurons are mapped by weight coefficient and deviation. According to the results, the value of weight coefficient and deviation are adjusted constantly to make the model error become very small, so as to get the final surrogate model [18].

Due to the different magnitude and range of each input parameter, if the input parameter is directly input into the

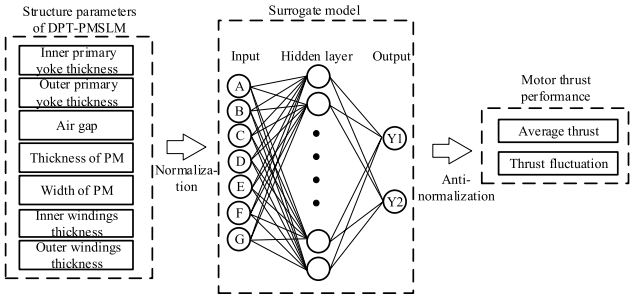

FIGURE 11. Structure diagram of neural network surrogate model.

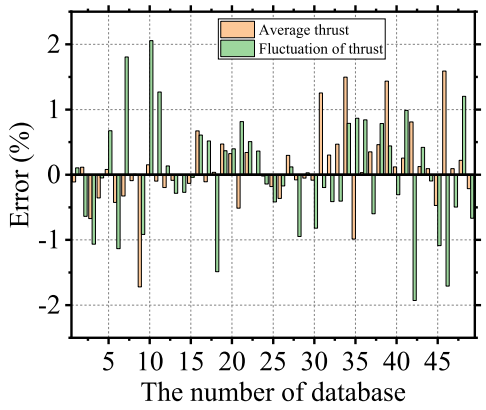

FIGURE 12. The error of the data.

hidden layer, the influence of different input parameters on the result is different, which reduces the accuracy of neural network. Therefore, each input parameter needs to be normalized to -1 ~1, where -1 represents the minimum value and 1 represents the maximum value within the parameter range, to ensure that each parameter has the same weight. A~G in Fig.11 are the normalized values of 7 inputs. Average thrust and thrust fluctuation are also different in order of magnitude. The output Y1 and Y2 of neural network will be between -1 ~1, and they can be anti-normalized to obtain the actual average thrust and thrust fluctuation values. Finally, 50 sets of motor schemes are generated randomly, and the results of the surrogate model and FEA are compared. The average thrust error between the surrogate model and FEA is less than 2%, as shown in Fig.12. Therefore, the surrogate model can predict the thrust performance of DPT-PMSLM within a reasonable error range.

B. PARETO FRONT METHOD FOR SOLVING MULTI-OBJECTIVE PROBLEMS

In view of the wide temperature range environment, a multi-objective optimization is carried out, and the thrust performance at different temperatures are studied. In order to make DPT-PMSLM have higher average thrust and lower thrust fluctuation, it is necessary to select the optimal structural parameters.

In this paper, a fast and simple random weighting method is used to solve the Pareto front. Firstly, a weighted evaluation

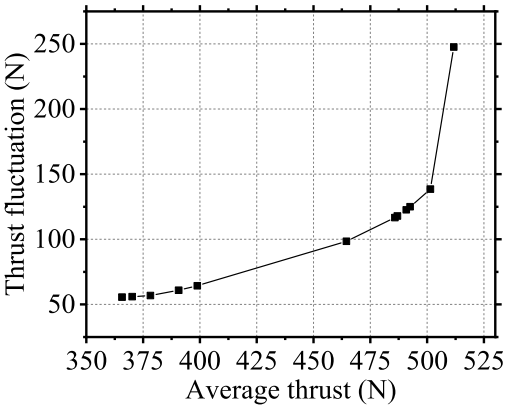

FIGURE 13. Pareto front of DPT-PMSLM.

function is established to transform multi-objective into single-objective. But the difference is that each goal is preceded by a random weight. Average thrust and thrust fluctuation are two main objectives. The evaluation function is established as

$$f_{\text{evalution}} = K \cdot F_{\text{Thrust}} - (1 - K) \cdot F_{\text{Thrust-ripple}} \quad (13)$$

where K is a random weight. Since the high average thrust and the low thrust fluctuation are required, the two are subtracted from the evaluation function.

Firstly, several lines are constructed by (13). Then the solution that maximizes the formula is obtained, which is the tangent point of each line and the point set. By selecting enough lines with different slopes, the set of tangent points is regarded as Pareto solution set, and its connecting line is taken as Pareto front. The approximate Pareto front can be obtained by a sufficient number of random K values. Pareto front is essentially a set of solutions which satisfy both high average thrust and low thrust fluctuation. Any point on it is the optimal solution, which can be selected according to the needs. Fig.13 shows one Pareto front of DPT-PMSLM.

C. MULTI-OBJECTIVE OPTIMIZATION OF DPT-PMSLM WITH WIDE ENVIRONMENT TEMPERATURE

The problem described in the previous section is a two-objective problem. In this paper, to get the final optimal solution, the influence of environment temperature on DPT-PMSLM needs to be considered. The effect of different temperature on motor is mainly manifested in the change of permanent magnet performance, which affects the thrust performance. Before multi-objective optimization considering environment temperature, design requirements and constraints should be determined. The wide temperature range of motor operation is ranging from -50°C to 50°C. The thrust performance of DPT-PMSLM at environment temperatures of -50°C, 20°C and 50°C and with the same structural parameters is shown in Table 2.

The Pareto front at different temperatures is also solved by the random weighting method. There are three design indexes: high average thrust, low thrust fluctuation and small

TABLE 2. Thrust performance at different temperatures before optimization.

Environment temperature (℃)	Average thrust(N)	Thrust fluctuation (N)
-50	453.16	133.17
20	422.34	114.01
50	408.23	106.35

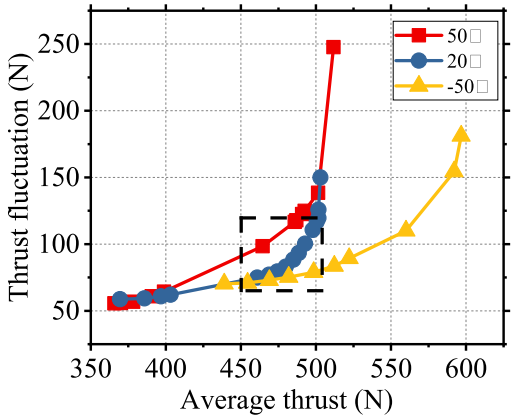

FIGURE 14. Optimization process 1.

variation of thrust at different temperatures. After the other two indexes reach reasonable values, the lower the thrust fluctuation, the better. The optimization is divided into four processes.

In process 1, the Pareto front of DPT-PMSLM at different temperatures is established in Fig.14. In order to meet the requirements of high average thrust and low thrust fluctuation, the scheme selection range needs to be specified. According to the tangents of Pareto front at 20°C and 50°C, the high average thrust range is selected, of which the right front is 503 N, the left front is 450 N. According to the lower tangent point of Pareto front at −50°C, the low thrust fluctuation range is selected, of which the lower front is 60 N, and the upper front is set as 120 N. These four fronts form a box to reduce the optimization interval. In the black box, the schemes in the upper left area of pareto front are all the alternatives that meet the current constraints.

In process 2, in order to meet the third performance requirement of small variation of thrust at different temperatures, the temperature-induced thrust changes are further constrained. If the variation of thrust at different required temperatures Ft is required to be less than 50N, the exhaustive method is used to search for points in the box area, and the points meeting the requirements at different temperatures are shown in Fig.15. Each point represents the average thrust and thrust fluctuation of DPT-PMSLM with a set of parameters.

In process 3, it is further required that Ft is less than 30N. All schemes that passed the screening are shown in Fig.16. It can be seen that after strengthening the constraints, the alternatives at −50°C are gradually concentrated in the upper area of the Fig.16, the alternatives at 20°C are concentrated

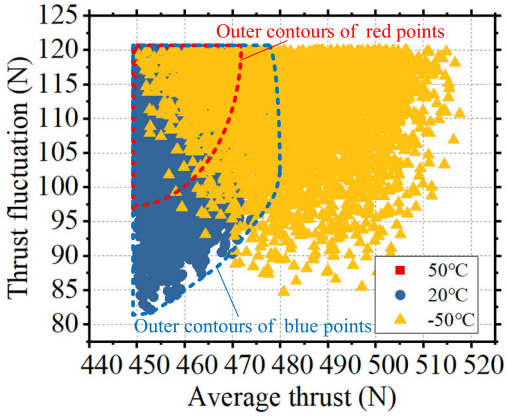

FIGURE 15. Optimization process 2.

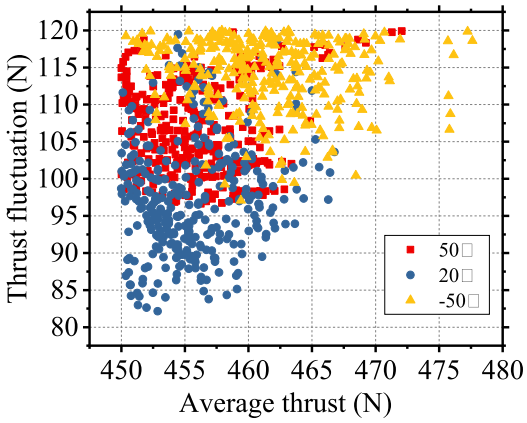

FIGURE 16. Optimization process 3.

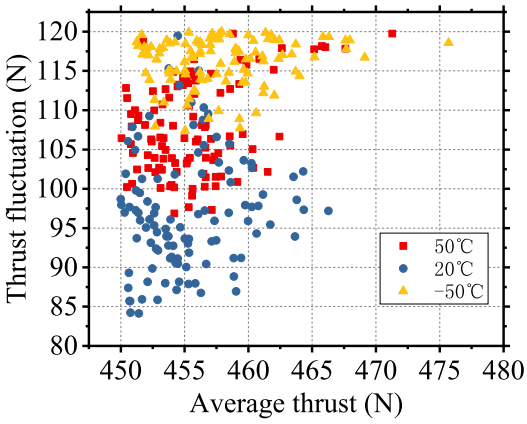

FIGURE 17. Optimization process 4.

in the lower left area, and the alternatives at 50°C are concentrated on the left area.

In process 4, Ft is set to be less than 20N. All schemes that passed the screening are shown in Fig.17. At this time, there are few alternatives that pass the screening. The above provides the premise that when the other two indexes reach reasonable values, the lower the thrust fluctuation, the better. Therefore, among the remaining schemes, the scheme with

TABLE 3. Optimized parameters of DPT-PMSLM.

parameters	Units	Values
Inner primary yoke thickness	mm	5.71
Outer primary yoke thickness	mm	3.63
Air gap	mm	0.82
Thickness of PM	mm	15.48
Width of PM	mm	15.83
Inner windings thickness	mm	9.54
Outer windings thickness	mm	10.00

TABLE 4. Thrust performance at different temperatures after optimization.

Environment temperature (℃)	Average thrust(N)	Thrust fluctuation (N)
-50	466.54	107.48
20	455.86	102.16
50	443.23	96.45

the minimum average thrust fluctuation is selected as the optimization result, as shown in Table 3.

In order to eliminate the error of surrogate model, the optimal thrust performance obtained by FEA is shown in Table 4. Compared with the initial structure, the thrust increases by 6.38% on average, the thrust fluctuation decreases by 13.42% on average, the maximum difference of thrust decreases by 48.12%.

IV. OPTIMIZATION OF END STRUCTURE

According to the result, the average thrust of DPT-PMSLM and the variation of thrust at different temperatures have reached optimal and reasonable values, but the thrust fluctuation still needs to be further restrained. The thrust fluctuation of linear motor mainly comes from the end effect [19]. If the end effect is taken into account when establishing the surrogate model, it will not be able to accurately reflect the specific influence of each structural parameter on the thrust fluctuation. Therefore, the end core optimization is not involved in the surrogate model. On the basis of the previous optimization results, this section optimizes end structure to restrain the thrust fluctuation of DPT-PMSLM.

A. CHANGE THE END LENGTH TO RESTRAIN DETENT FORCE

The end detent force can be changed by changing the end length of primary core [20]. The structural drawing of end core with double primary structure is shown in Fig.18. To maintain symmetry, the changes at both ends of each primary are the same. The extension value of one side in outer primary end is L_1, and that in inner primary end is L_2.

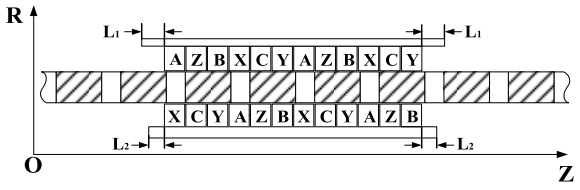

FIGURE 18. End structure drawing of DPT-PMSLM.

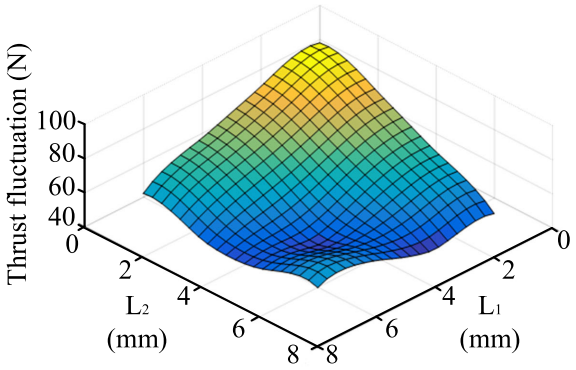

FIGURE 19. When L1and L2 are unequal, the relationship between end length and thrust fluctuation.

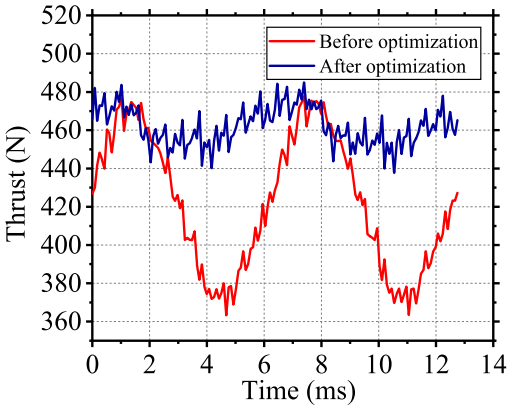

FIGURE 20. Thrust waveforms before and after changing the end length at 20 °C.

The length of outer and inner ends has different influence on the overall detent force of DPT-PMSLM, so it is necessary to choose different L_1 and L_2 for optimization. Select the ends of different lengths and simulate them with FEA method. The value of thrust fluctuation is shown in Fig.19.

It can be seen that, in the optimal solution, L_1 is 5.5mm, L_2 is 5mm. Finally, the average thrust is 461.60 N at 20 °C, which is increased by 5.74 N. And the thrust fluctuation is 43.62 N, which is reduced by 58.54 N. Fig.20 shows the thrust waveform comparison of DPT-PMSLM before and after changing the end length.

B. AXIAL DISPLACEMENT TO RESTRAIN DETENT FORCE

According to the end detent force characteristics of linear motor, the phase of outer and inner primary motors' detent can be adjusted by axial displacement [21]. By offsetting each

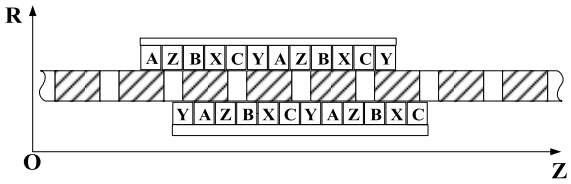

FIGURE 21. A phase sequence diagram of windings with axial displacement structure.

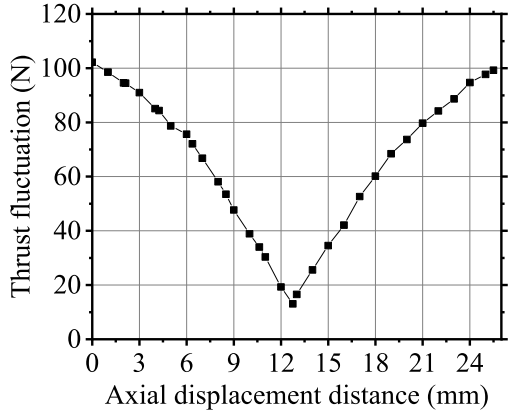

FIGURE 22. Influence of axial displacement distance on thrust fluctuation.

other, the end detent force can be reduced. However, this method can not only restrain detent force, but also change the spatial electrical angle of windings, thus affecting output thrust. Therefore, it is necessary to adjust the phase of windings when using axial displacement structure, so as to restrain detent force without losing much average thrust at the same time [22]. Fig.21 is a phase sequence diagram of windings with axial displacement structure.

The DPT-PMSLM is 4-pole and 12-slot, and the electric angle of two adjacent slots is 60°. During axial displacement, ensure that the outer windings stay still, and the inner windings move with the primary. It can be seen that when the moving distance of inner winding reaches 1/3 of a pole distance, the back EMF of inner windings is $180*1/3 = 60°$ ahead of the outer windings. At this time, if the phase sequence of inner windings is not changed, there will be phase difference between the three-phase back EMF of outer and inner windings, and the thrust of DPT-PMSLM will be lost to a certain extent. Therefore, the phase sequence of windings is changed to make up for the influence of axial displacement.

When adjusting the axial displacement distance, choose the phase sequence which can minimize the thrust fluctuation. The main source of the thrust fluctuation of the motor is the detent force, and the other part is the fluctuation caused by the phase sequence deviation of the axial displacement winding. Fig.22 shows the influence of axial displacement distance on thrust fluctuation.

It can be seen that when the axial displacement is 12.75mm, there is a minimum value, which is consistent with the theoretically 0.5 times the pole pitch τ. At this time, combined with the phase sequence adjustment of winding,

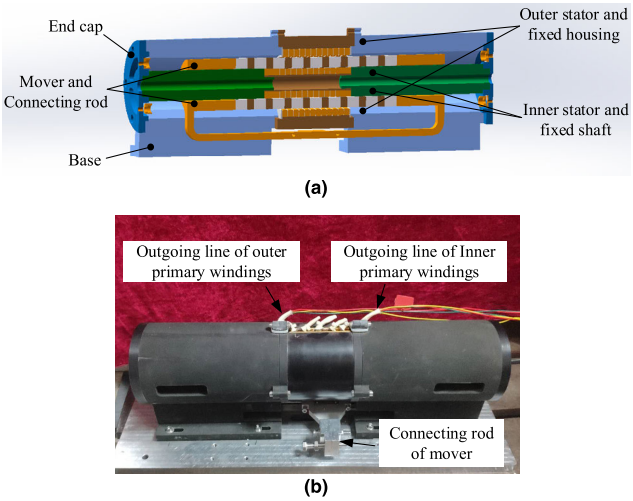

FIGURE 23. Prototype. (a) 3D sectional view. (b) Appearance.

according to the finite element simulation, the thrust fluctuation is 13.06 N, which is reduced by 89.06 N. But the average thrust is also reduced by 20.51 N inevitably and becomes 435.35 N now.

Comparing the above two methods, changing end length can restrain the thrust fluctuation, improve the utilization ratio of iron core and make the thrust rise slightly, which is suitable for the applications with strict requirements on output thrust. The method of axial displacement is much better than the former in restraining the thrust fluctuation, but it will lose a small part of thrust, which is suitable for the applications with strict requirements on thrust fluctuation.

V. PROTOTYPE AND EXPERIMENT

In order to verify the effectiveness of work in this paper, a DPT-PMSLM prototype is developed and an experimental test platform is built. The detent force and the static thrust are tested.

Each primary of the prototype adopts four poles and twelve slots, a total of 24 slots. The method of axial displacement is chosen to restrain detent force. The outer and inner primary are fixed, and the secondary is placed on the guide rail by the connection mechanism. The supporting structure at both ends fixes outer and inner primary winding wires. The outer primary windings lead out from the upper hole, and the inner primary windings lead out from the hollow central axis. The 3D sectional view and the appearance of prototype are shown in Fig.23. And the experimental platform is set up as shown in Fig.24.

In order to measure the detent force of DPT-PMSLM, a tension pressure sensor is used in this paper, which can convert thrust into a voltage signal. Firstly, the tension pressure sensor with appropriate range needs to be installed between the connector and the servo cylinder. In this paper, a tension pressure sensor with a range of 50 N is adopted. By driving the servo cylinder to drive DPT-PMSLM, the oscilloscope receives the voltage signal of tension sensor in the process of movement.

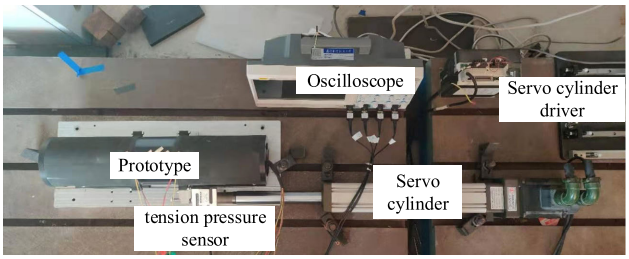

FIGURE 24. Prototype and experimental platform.

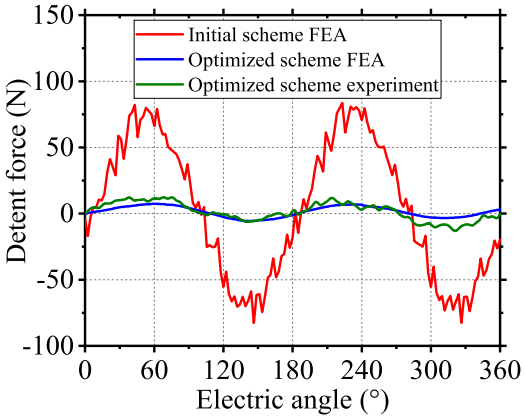

FIGURE 25. Detent force waveform.

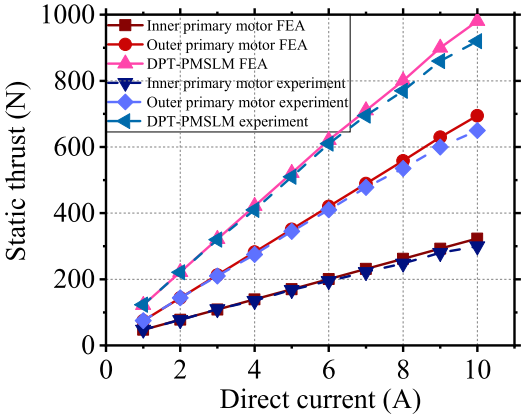

FIGURE 26. Law of static thrust changing with DC current.

Finally, according to the corresponding ratio on the nameplate of tension pressure sensor, voltage signal is converted into the waveform of thrust. The simulation and experimental detent force waveform vary with electrical angle as shown in Fig.25.

It can be seen that the detent force of DPT-PMSLM is obviously restrained after optimization. The experiment value of detent force is slightly higher than the design value. This is due to machining inaccuracy, such as error between the actual axial displacement distance and the design value.

To test DPT-PMSLM's static thrust, parallel B-phase and C-phase, and then reverse series with A-phase. A-phase winding is passed with a given positive DC current, B-phase and C-phase are passed with negative DC current, of which the value is half of that in phase A. In this case, the effective value of three-phase winding is equal to the given DC current value divided by the square root of 2. Generally, static thrust waveform is sine wave, and static thrust is the maximum value of waveform in one period. Fig.26 shows the variation rule of static thrust with DC current.

It can be seen that when DC current value is less than 7 A, the static thrust test values of outer, inner and DPT-PMSLM are basically the same as the FEA simulation values; when DC current continues to increase, the static thrust test values are less than the FEA simulation values. The main reason is also the inaccuracy of axial displacement distance in machining, so a part of thrust is lost.

VI. CONCLUSION

In this paper, a DPT-PMSLM is taken as the research object. The equivalent magnetic circuit model is established, the law of electromagnetic and thrust characteristics changing with electromagnetic parameters is analyzed. Then a surrogate model is established by neural network to simplify the complex mathematical derivation process of DPT-PMSLM's thrust characteristics. The multi-objective optimization based on Pareto front method and the end core optimization are adopted. After optimization, the average thrust of DPT-PMSLM at 20°C is more than 430N, the thrust fluctuation is reduced by 88.5%, and the average thrust difference decreases to 23.31 N within the range of $-50°C \sim 50°C$, which is 48.1% lower than the initial scheme. The experimental results are close to the simulation results, which proves the effectiveness of the optimization.

REFERENCES

[1] A. Musolino, M. Raugi, R. Rizzo, and M. Tucci, "Optimal design of EMALS based on a double-sided tubular linear induction motor," *IEEE Trans. Plasma Sci.*, vol. 43, no. 5, pp. 1326–1331, May 2015.

[2] J. Prudell, M. Stoddard, T. K. A. Brekken, and A. von Jouanne, "A novel permanent magnet tubular linear generator for ocean wave energy," in *Proc. IEEE Energy Convers. Congr. Expo.*, San Jose, CA, USA, Sep. 2009, pp. 3641–3646.

[3] H. Chen, W. Yan, J. J. Gu, and M. Sun, "Multiobjective optimization design of a switched reluctance motor for low-speed electric vehicles with a Taguchi–CSO algorithm," *IEEE/ASME Trans. Mechatronics*, vol. 23, no. 4, pp. 1762–1774, Aug. 2018.

[4] J. H. Lee, J.-Y. Song, D.-W. Kim, J.-W. Kim, Y.-J. Kim, and S.-Y. Jung, "Particle swarm optimization algorithm with intelligent particle number control for optimal design of electric machines," *IEEE Trans. Ind. Electron.*, vol. 65, no. 2, pp. 1791–1798, Feb. 2018.

[5] H. Gu, L. Yang, Z. Hu, and J. Yu, "Surrogate models for shape optimization of underwater glider," in *Proc. Int. Conf. Comput. Model. Simul.*, Feb. 2009, pp. 3–6.

[6] W. Qin, J. Dong, Y. Li, and M. Wang, "Fast multi-objective antenna design based on BPNN surrogate model," in *Proc. Int. Appl. Comput. Electromagn. Soc. Symp.-China (ACES)*, Beijing, China, Jul. 2018, pp. 1–2.

[7] S. S. Miriyala, P. Devi Pantula, S. Majumdar, and K. Mitra, "Enabling online optimization and control of complex models through smart surrogates based on ANNs," in *Proc. Indian Control Conf. (ICC)*, Jan. 2016, pp. 214–221.

[8] L. Ortombina, F. Tinazzi, and M. Zigliotto, "Magnetic modeling of synchronous reluctance and internal permanent magnet motors using radial basis function networks," *IEEE Trans. Ind. Electron.*, vol. 65, no. 2, pp. 1140–1148, Feb. 2018.

[9] N. Javadian, A. Mozdgir, E. G. Kouhi, D. Qajar, and M. E. Shiraqai, "Solving assembly flowshop scheduling problem with parallel machines using variable neighborhood search," in *Proc. Int. Conf. Comput. Ind. Eng.*, Jul. 2009, pp. 102–107.

[10] A. Allahverdi and F. S. Al-Anzi, "Evolutionary heuristics and an algorithm for the two-stage assembly scheduling problem to minimize makespan with setup times," *Int. J. Prod. Res.*, vol. 44, no. 22, pp. 4713–4735, 2006.

[11] Y. Yang, J.-F. Wu, X.-B. Zhu, and J.-C. Wu, "A hybrid evolutionary algorithm for finding Pareto optimal set in multi-objective optimization," in *Proc. 7th Int. Conf. Natural Comput.*, Jul. 2011, pp. 1233–1236.

[12] Z.-H. Zhou and Z.-C. Yang, "Stochastic characteristic analysis of turbine rotor based on response surface method," in *Proc. 2nd Int. Conf. Ind. Mechatronics Autom.*, May 2010, pp. 138–141.

[13] H.-Y. Lee, E.-C. Lee, G.-J. Lee, and S.-O. Kwon, "Evaluation of slotless permanent synchronous motor with toroidal winding," in *Proc. IEEE Energy Convers. Congr. Expo. (ECCE)*, Baltimore, MD, USA, Sep. 2019, pp. 1735–1738.

[14] Y.-G. Liu, X. Zhu, and X.-P. Li, "A new hybrid genetic algorithm for the bi-criteria no-wait flowshop scheduling problem with makespan and total flow time minimization," in *Proc. Int. Conf. Mach. Learn. Cybern.*, Jul. 2008, pp. 883–888.

[15] N. Bianchi, S. Bolognani, D. Dalla Corte, and F. Tonel, "Tubular linear permanent magnet motors: An overall comparison," *IEEE Trans. Ind. Appl.*, vol. 39, no. 2, pp. 466–475, Mar. 2003.

[16] J. Wang, G. W. Jewell, and D. Howe, "Design optimisation and comparison of tubular permanent magnet machine topologies," *IEE Proc.-Electr. Power Appl.*, vol. 148, no. 5, pp. 456–464, Sep. 2001.

[17] J. Ji, Z. Ling, J. Wang, W. Zhao, G. Liu, and T. Zeng, "Design and analysis of a Halbach magnetized magnetic screw for artificial heart," *IEEE Trans. Magn.*, vol. 51, no. 11, pp. 1–4, Nov. 2015.

[18] O. Rahmani, M. Iltarabian, and S. A. Sadrossadat, "Modeling and simulation of speed and efficiency of BLDC motor as a starter motor based on multilayer perceptron (MLP) neural network," in *Proc. IEEE Transp. Electrific. Conf. Expo, Asia–Pacific (ITEC Asia–Pacific)*, Bangkok, Thailand, Jun. 2018, pp. 1–5.

[19] K. Jang, J. Kim, H. An, and G. Kim, "Optimal design of auxiliary teeth to minimize unbalanced phase due to end effect of PMLSM," *IEEE Trans. Magn.*, vol. 47, no. 5, pp. 1010–1013, May 2011.

[20] J. Hu, F. Liu, and Y. Li, "Investigation of reducing end detent force in PM linear synchronous motor using multi-unit technique," in *Proc. 22nd Int. Conf. Electr. Mach. Syst. (ICEMS)*, Harbin, China, Aug. 2019, pp. 1–5.

[21] J. Li, X. Huang, Q. Tan, and Z. Qian, "Thrust optimization of permanent magnet synchronous linear motor based on tooth-shifting of double sides," in *Proc. 19th Int. Conf. Elect. Mach. Syst. (ICEMS)*, Chiba, Japan, Nov. 2016, pp. 1–5.

[22] J. Li, X. Huang, B. Zhou, H. Yu, and Q. Huang, "Design principle of a 16-pole 18-slot two-sectional modular permanent magnet linear synchronous motor with optimisation of its end tooth," *IET Electr. Power Appl.*, vol. 14, no. 3, pp. 441–447, Mar. 2020.